Sensors and Materials, Vol. 38, No. 3 (2026) 1135–1152
MYU Tokyo

S & M 4368

Robust Estimation of Noncontact Vital Sign Sensing Data under Multi-source Dynamic Interference Scenarios

Ning Wang,[1,2] Hongqing Li,[2] Zhiwei Li,[1] Wentong Gao,[2]
Jingyi An,[2] Yuting Pai,[2] and Yiqiang Zhao[1*]

[1]School of Microelectronics, Tianjin University, Tianjin 300072, China
[2]Tianjin Jianjun Technology Co., Ltd., Tianjin 300000, China

(Received November 7, 2025; accepted February 3, 2026)

Keywords: multi-source dynamic interference, millimeter-wave radar, vital sign monitoring, Chameleon Swarm Algorithm, Successive Variational Mode Decomposition

Millimeter-wave radar noncontact vital sign sensors are widely used in home care and clinical monitoring. However, in practical applications, these sensors face multi-source dynamic interferences such as motion artifacts, environmental vibrations, and electromagnetic noise, leading to a severe degradation in estimation accuracy. To address this issue, we propose a Chameleon Swarm Algorithm-assisted Optimized Successive Variational Mode Decomposition (CSA-SVMD) algorithm in this paper. The algorithm constructs a fitness function based on the time-frequency domain characteristics of vital sign signals, utilizes the Chameleon Swarm Algorithm to achieve the adaptive optimization of the balancing parameter in Successive Variational Mode Decomposition, and finally realizes the accurate estimation of vital signs by combining frequency priors and magnitude-squared coherence. This approach ensures estimation accuracy while significantly enhancing robustness against multi-source dynamic interference. Experimental results based on the BMR2 vital sign monitoring board show that the CSA-SVMD algorithm achieves a root mean square error (*RMSE*) of about 2 beat per minute (bpm) for respiratory rate and about 3 bpm for heart rate at a distance of 0.5 m across all tested subjects. Although *RMSE* increases with measurement distance, the algorithm maintains a stable performance degradation trend in multi-source dynamic interference scenarios.

1. Introduction

Millimeter-wave radar noncontact vital sign monitoring technology, based on noninvasive sensing principles, not only ensures reliable privacy protection and all-weather monitoring capabilities but also allows raw radar signals to be processed to extract more centralized information for medical applications, such as detecting changes in breathing and heartbeat to predict disease at an early stage.[1,2] Because it effectively resolves issues such as skin irritation from contact-based measurements, this technology is particularly suitable for the long-term monitoring of special populations such as burn patients, the elderly with limited mobility, and

*Corresponding author: e-mail: yq_zhao@tju.edu.cnt
https://doi.org/10.18494/SAM5993

ISSN 0914-4935
https://myukk.org/

infants, demonstrating significant advantages in clinical auxiliary diagnosis and home-based health management.[3–5]

In practical monitoring scenarios, millimeter-wave radar is subject to multi-source dynamic interferences, including motion artifacts, environmental vibrations, and electromagnetic noise. The interference signals overlap with vital sign signals in both the time and frequency domains, degrading the performance of traditional spectral analysis methods and consequently leading to inaccurate vital sign monitoring data. To estimate vital sign signals under multi-source dynamic interference scenarios, techniques such as wavelet transform (WT),[6] empirical mode decomposition (EMD),[7] and variational mode decomposition (VMD)[8,9] are commonly employed. Li *et al.*[10] proposed an enhanced empirical WT algorithm for the adaptive decomposition and reconstruction of vital sign signals, which integrates the adaptive decomposition concept of EMD with the compact support framework of WT theory. By employing a Sparrow Search Algorithm (SSA) and fuzzy entropy, the method identifies optimal spectral boundaries. However, the algorithm is constrained by the spectral separability assumption, where spectral segmentation relies on the presence of significant spectral extrema points. If the spectral amplitude difference between vital signs and noise signals is minimal, this may lead to erroneous segmentation. To address the susceptibility of vital sign signals to interference, Zuo[11] employed VMD for the separation and reconstruction of respiratory and cardiac signals. The algorithm uses a swarm decomposition algorithm to adaptively adjust the number of modes and the penalty factor. A limitation is that the algorithm does not account for coupling effects among multiple optimization objectives. Li *et al.*[12] utilized successive VMD (SVMD)[13] to extract heartbeat signals from vital signs. The SVD-FOCUSS-Recovery algorithm was applied to estimate heartbeat frequency. A drawback of this approach is that it lacks a mechanism for the adaptive optimization of its balancing parameter, which can result in mode aliasing or incomplete decomposition, thereby affecting the accuracy of the final heartbeat frequency estimation.

To address the issues of low estimation accuracy and robustness of vital sign signals under multi-source dynamic interference scenarios, we propose a Chameleon Swarm Algorithm-assisted Optimized Successive Variational Mode Decomposition (CSA-SVMD) algorithm in this paper. The algorithm constructs a fitness function based on the time-frequency domain features of vital sign signals. It employs the Chameleon Swarm Algorithm (CSA)[14] for the adaptive optimization of the key parameter in SVMD. Finally, it combines frequency priors and magnitude-squared coherence (MSC) to precisely estimate vital sign signals. This approach effectively mitigates inaccuracies in vital sign monitoring caused by the coupling of motion artifacts, environmental vibrations, and electromagnetic noise. Thereby, it enhances the estimation accuracy and robustness of vital sign signals in multi-source dynamic interference scenarios.

2. Methods

2.1 Millimeter-wave radar for vital sign estimation

Millimeter-wave radar enables the noncontact monitoring of vital signs by transmitting frequency-modulated continuous wave (FMCW) signals and receiving echoes reflected from the human.[15] Figure 1 shows the principle of FMCW radar-based vital sign sensing.

The transmitted signal $S_T(t)$ can be expressed as

$$S_T(t) = A_T e^{j\left(2\pi f_c t + \pi \frac{B}{T} t^2 + \varphi_0\right)}, \tag{1}$$

where A_T is the amplitude of the transmitted signal, f_c is the initial frequency, B is the signal bandwidth, T is the duration of each chirp, and φ_0 is the initial phase.

The received signal $S_R(t)$ by the radar exhibits a time delay, $\tau = 2R/c$ proportional to the target distance R relative to the transmitted signal (c being the speed of light). By mixing the received signal with the transmitted signal, an intermediate frequency (IF) signal $S_{IF}(t)$ containing both target distance and micro-motion information is obtained:

$$S_{IF}(t) = A_{IF} e^{j(f_{IF} t + \varphi_{IF})}, \tag{2}$$

where A_{IF} is the amplitude of the IF signal, $f_{IF} = 4\pi BR/cT$ is the frequency, $\varphi_{IF} = 4\pi R/\lambda$ is the phase, and λ is the wavelength.

Target detection is achieved by performing a fast Fourier transform (FFT)[16] on the IF signal, and phase demodulation and unfolding are then applied to the corresponding range bin to extract the phase signal's temporal variation. The time-varying phase of the target's IF signal under continuous monitoring is expressed as

$$\varphi_d(t) = 4\pi \frac{d_0 + d(t)}{\lambda}, \tag{3}$$

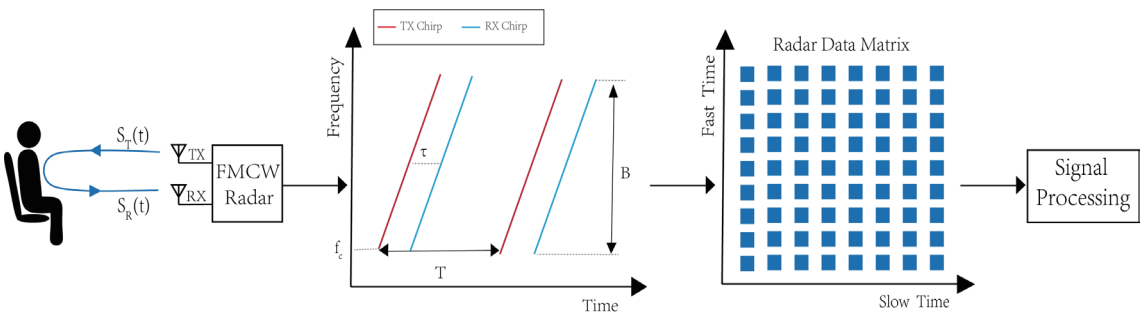

Fig. 1. (Color online) Principle of FMCW radar-based vital sign sensing.

where d_0 is the fixed distance between the radar and the target, and $d(t)$ is the chest displacement induced by respiration and heartbeat.

Both respiration and heartbeat induce periodic micro-displacements of the chest surface, and their motion characteristics can be approximated as sinusoidal oscillations. The chest displacement signal $d(t)$ caused by respiration and heartbeat can be modelled as

$$d(t) = A_r\cos(2\pi f_r t + \varphi_r) + A_h\cos(2\pi f_h t + \varphi_h) + n(t), \tag{4}$$

where A_r, f_r, and φ_r are the amplitude, frequency, and phase of the respiratory signal, respectively; A_h, f_h, and φ_h are the corresponding parameters of the cardiac signal; and $n(t)$ is the noise and interference signal.

The phase of the IF signal $\varphi_d(t)$ is essentially a composite of respiration, heartbeat, and interference. By analyzing its variation characteristics to extract the respiratory and cardiac signals, millimeter-wave radar-based vital sign estimation can be achieved. In practical applications, direct extraction is challenging owing to the superposition of respiratory and cardiac signals and the effect of interference signals. The proposed CSA-SVMD algorithm is designed for the precise estimation of vital sign signals during continuous monitoring under multi-source dynamic interference scenarios.

2.2 SVMD

SVMD is an adaptive signal decomposition method suited for processing nonstationary and nonlinear signals. It does not need to set the mode number, and the optimization objective is improved further to emphasize the narrowband property of the decomposition results.[17] It achieves this by treating each mode as a signal with a maximally compact spectrum, ensuring minimal spectral overlap with other modes and the residual. This prevents convergence towards previously extracted modes.

The decomposition of the input signal $f(t)$ into the Lth mode $u_L(t)$ and the residual signal $f_r(t)$ is expressed as

$$f(t) = u_L(t) + f_r(t)\,. \tag{5}$$

The residual signal $f_r(t)$ comprises the sum of all previously extracted modes $\sum_{i=1}^{L-1} u_i(t)$ and the remaining unprocessed portion of the input signal $f_u(t)$.

The SVMD extracts each mode based on four constraints, formulated as follows.

2.2.1 Spectral compactness constraint J_1

This constraint ensures that each extracted mode $u_L(t)$ has a maximally compact spectrum around its center frequency ω_L. It is expressed as

$$J_1 = \left\| \partial_t \left[\left(\delta(t) + \frac{j}{\pi t} \right) * u_L(t) \right] e^{-j\omega_L t} \right\|_2^2, \tag{6}$$

where * denotes the convolution operation.

2.2.2 Residual spectral overlap minimization constraint J_2

To minimize spectral overlap between the current mode $u_L(t)$ and the residual signal $f_r(t)$, a frequency-domain filter $\hat{\beta}_L(\omega)$ is applied to the residual. The filter's frequency response is designed to attenuate components around the current mode's center frequency and is expressed as

$$\hat{\beta}_L(\omega) = \frac{1}{\alpha(\omega - \omega_L)^2}. \tag{7}$$

The constraint minimizes the energy of the filtered residual and is expressed as

$$J_2 = \left\| \beta_L(t) * f_r(t) \right\|_2^2, \tag{8}$$

where $\beta_L(t)$ is the impulse response of the filter described in Eq. (7).

2.2.3 Separation from previous modes constraint J_3

This constraint prevents the newly extracted mode $u_L(t)$ from converging to any of the previously extracted modes $u_i(t)$ (for $i = 1, 2, ..., L-1$). Similar filters are applied to the current mode around the center frequencies of past modes, and their response is expressed as

$$\hat{\beta}_i(\omega) = \frac{1}{\alpha(\omega - \omega_i)^2}. \tag{9}$$

The constraint minimizes the sum of energies from these filtering operations and is expressed as

$$J_3 = \sum_{i=1}^{L-1} \left\| \beta_i(t) * u_L(t) \right\|_2^2, \tag{10}$$

where $\beta_i(t)$ is the impulse response of the filter described in Eq. (9).

2.2.4 Reconstruction fidelity constraint

This ensures that the sum of the current mode $u_L(t)$, the unprocessed signal portion $f_u(t)$, and all previously extracted modes perfectly reconstructs the original input signal:

$$f(t) = u_L(t) + f_u(t) + \sum_{i=1}^{L-1} u_i(t). \tag{11}$$

In each decomposition step, SVMD extracts the Lth mode by solving the following constrained optimization problem, which combines all constraints with a balancing parameter α. It is expressed as

$$\begin{aligned} &\min_{u_L, \omega_L, f_r} \{\alpha J_1 + J_2 + J_3\} \\ &\text{s.t. } u_L(t) + f_r(t) = f(t). \end{aligned} \tag{12}$$

The parameter α balances the trade-off among the three constraints. A higher α emphasizes narrowband modes but may increase sensitivity to noise, while a lower α may lead to mode mixing.

This constrained problem is solved by introducing an augmented Lagrangian function and employing the Alternating Direction Method of Multipliers for an iterative optimization. The process iteratively extracts dominant modal components until the residual energy falls below a predefined threshold or all dominant modes are recovered.

2.3 CSA

CSA is a highly efficient meta-heuristic optimizer proposed in recent years. It is inspired by the dynamic foraging strategies of chameleons during hunting, which include global search, eye movement coordination for tracking, and rapid prey capture via tongue projection. Unlike traditional gradient-based methods, CSA is gradient-free and suitable for black-box optimization, nonlinear, and nonconvex problems. The algorithm simulates chameleons' independent eye rotation for precise local exploitation, affine planar search combined with random exploration for robust global search, and tongue attack simulation for accelerated convergence. This enables an adaptive balance between exploration and exploitation, making CSA particularly effective in complex, high-dimensional search spaces. As a result, CSA has demonstrated significant performance advantages in solving complex optimization problems, owing to its exceptional global exploration capability, precise local exploitation, and convergence stability.

2.3.1 Initialization

The initial population of n chameleons is generated by randomly sampling positions within the d-dimensional search space, forming a population matrix y of size $n \times d$. The position of the ith chameleon ($i = 1, 2, ..., n$) at iteration t is denoted as

$$\boldsymbol{y}_t^i = \left[\boldsymbol{y}_{t,1}^i, \boldsymbol{y}_{t,2}^i, ..., \boldsymbol{y}_{t,j}^i, ..., \boldsymbol{y}_{t,d}^i \right], \tag{13}$$

where $i = 1, 2, ..., n$, t is the current iteration number, d stands for the dimension of the problem,

and $\boldsymbol{y}_{t,d}^{i}$ denotes the position of the ith chameleon at the dth dimension. Each chameleon's position represents a candidate solution, i.e., the parameter α to be optimized.

2.3.2 Search for prey

The chameleon's foraging behavior during the global exploration phase is mathematically modeled by the following position update strategy, which is governed by a perception probability, mathematically modelled as

$$\boldsymbol{y}_{t+1}^{i,j} = \begin{cases} \boldsymbol{y}_t^{i,j} + p_1(P_t^{i,j} - G_t^i)r_2 + p_2(G_t^j - \boldsymbol{y}_t^{i,j})r, & r_i \geq P_p \\ \boldsymbol{y}_t^{i,j} + \boldsymbol{\mu}((u^j - l^j)r_3 + l_b^j)\mathrm{sgn}(rand - 0.5), & r_i < P_p \end{cases}, \tag{14}$$

where $P_t^{i,j}$ is the best position that has scored so far by chameleon i in the jth dimension at iteration loop t, G_t^j is the global best position in the jth dimension obtained so far by any chameleon in the tth iteration, p_1 and p_2 are two positive numbers that control exploration ability, r_1, r_2, and r_3 are random numbers generated uniformly in the range of [0,1], r_i is a random number generated uniformly at index i at the interval [0,1], $\mathrm{sgn}(rand - 0.5)$ has an effect on the direction of exploration and exploitation, and it can be either 1 or −1, and i is a parameter defined as a function of iterations that decreases with the number of iterations.

2.3.3 Chameleon eyes' rotation

Upon prey detection, the chameleon accurately locks onto the target through eye rotation. This behavior corresponds to the local exploitation phase of the algorithm. The position update formula is

$$\boldsymbol{y}_{t+1}^{i} = \boldsymbol{m} \times (\boldsymbol{y}_t^i - \overline{\boldsymbol{y}}_t^i) + \overline{\boldsymbol{y}}_t^i, \tag{15}$$

where $\overline{\boldsymbol{y}}_t^i$ is the center of the current position of the chameleon before rotation and $\boldsymbol{m}$ is a rotation matrix. This operation allows the chameleon to perform a refined search around the current optimal region, which enhances the accuracy of the solution.

2.3.4 Hunting prey

When the solution approaches (near-)optimality, the algorithm mimics the chameleon's rapid prey capture via tongue projection by employing a velocity update mechanism to accelerate convergence:

$$v_{t+1}^{i,j} = \omega\, v_t^{i,j} + c_1(G_t^i - \boldsymbol{y}_t^{i,j})\, r_1 + c_2\, (P_t^{i,j} - \boldsymbol{y}_t^{i,j})r_2, \tag{16}$$

$$\boldsymbol{y}_{t+1}^{i,j} = \boldsymbol{y}_t^{i,j} + \frac{(v_t^{i,j})^2 - (v_{t-1}^{i,j})^2}{2\eta}, \tag{17}$$

where $v_t^{i,j}$ is the current velocity of the ith chameleon in the jth dimension, c_1 and c_2 are two positive constants that control the effects of $P_t^{i,j}$ and G_t^j on dropping the chameleon's tongue, r_1 and r_2 are two random numbers distributed in the range from 0 to 1, ω is the inertia weight, and η is the acceleration rate of the chameleon's tongue projection.

Compared with mainstream meta-heuristic algorithms such as the Grey Wolf Optimizer (GWO), Moth Flame Optimization (MFO), and SSA, CSA demonstrates statistically superior performance across unimodal, multimodal, hybrid, and composite benchmark functions. In extensive evaluations on 67 test functions, CSA consistently achieves lower mean fitness and standard deviation values, particularly in multimodal and composite categories such as CEC-2017, where it outperforms GWO, MFO, and SSA in 26 out of 29 functions. This robustness stems from CSA's dynamic balance between exploration and exploitation, making it particularly effective in high-dimensional and constrained optimization problems.

2.4 CSA-SVMD algorithm

To accurately estimate vital signs under multi-source dynamic interference scenarios, we propose a CSA-SVMD algorithm in this paper. The core of the algorithm lies in adaptively optimizing the balancing parameter of SVMD using CSA, constructing a fitness function based on the time-frequency characteristics of vital sign signals, and accurately extracting respiratory and cardiac signals by incorporating frequency priors and MSC,[18] thereby enabling the precise estimation of vital sign parameters. The execution flow of the proposed algorithm is illustrated in Fig. 2.

The algorithm begins by initializing the relevant parameters of CSA and the SVMD balancing parameter; then, an initial population is randomly generated to initiate the optimization process. CSA iteratively searches for the optimal balancing parameter. For each candidate parameter, the algorithm performs SVMD, evaluates the fitness of the output modes, and uses this fitness to guide the search toward minimization. If the current fitness value is lower than the historical optimum, we update the optimal balancing parameter and their fitness value. We repeat the above steps until the maximum iteration count is reached, then we output the globally optimal balancing parameter and the optimal fitness value.

The specific steps for calculating the fitness value are as follows.

To effectively evaluate the decomposition performance of the SVMD balancing parameter, a fitness function that reflects the intrinsic characteristics of vital sign signals is constructed. In this study, we design a comprehensive evaluation metric that integrates a bandwidth penalty term and envelope entropy based on the narrowband characteristics of respiratory and cardiac signals in the frequency domain and their sparsity in the time domain.

Given that vital sign signals exhibit energy highly concentrated around their fundamental frequency, the following procedure is applied to each candidate balancing parameter during

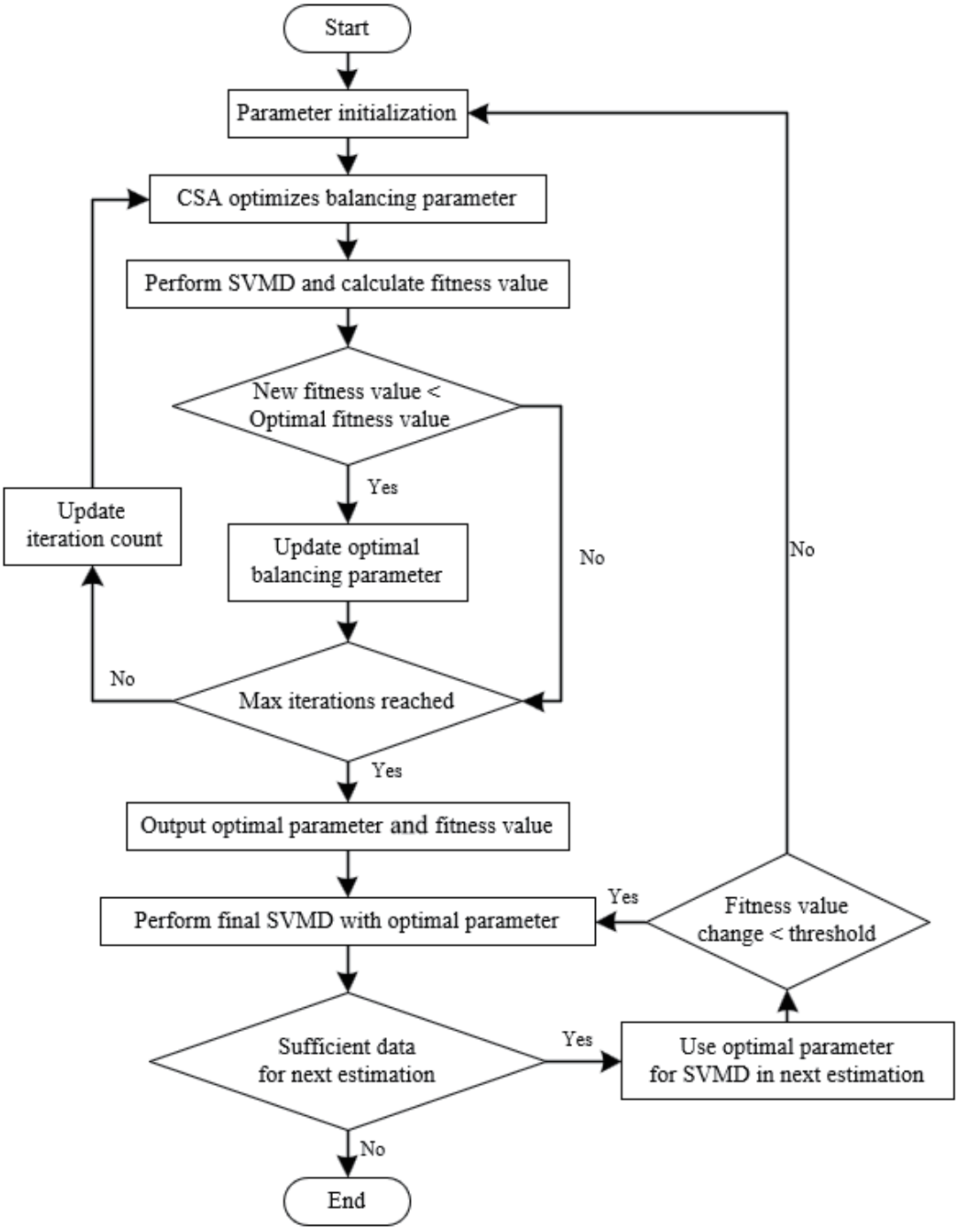

Fig. 2. Flowchart of CSA-SVMD algorithm.

iteration. First, the decomposed modal component $u_k(t)$ $(k = 1, 2, ..., K)$ is Fourier-transformed to obtain the frequency spectra $U_k(f)$. The power spectral density (PSD)[19] is then computed, and the actual bandwidth B_k of each component is determined on the basis of cumulative energy thresholds. The bandwidth penalty term $P(B_k)$ quantifies the deviation of the measured bandwidths from the prior expected range $[B_{min}, B_{max}]$ for vital signs and is defined as

$$P(B_k) = \begin{cases} 0, & \text{if } B_k \in [B_{min}, B_{max}] \\ B_k - B_{max}, & \text{if } B_k > B_{max} \\ B_{min} - B_k. & \text{if } B_k < B_{min} \end{cases} . \tag{18}$$

To quantify the noise level and waveform purity of modal components, envelope entropy is employed as a quantitative measure of its sparsity in the time domain. The envelope signal $a(j)$ is first obtained by applying the Hilbert transform to the modal component $u_k(t)$, and envelope entropy is then defined as the information entropy of the normalized probability distribution p_j derived from this envelope signal:

$$E_k = -\sum_{j=1}^{N} p_j \log(p_j). \tag{19}$$

A lower envelope entropy value indicates a higher concentration of signal energy in the time domain, which corresponds to a reduced noise interference in the corresponding modal component.

The final fitness function is the weighted sum of the above two metrics:

$$Fitness = \sum_{k=1}^{K} (\omega_1 P(B_k) + \omega_2 E_k), \tag{20}$$

where K is the total number of modes and ω_1 and ω_2 are the weighting coefficients that satisfy $\omega_1 + \omega_2 = 1$, balancing the contributions of the frequency-domain and time-domain metrics. The optimization objective is to minimize the fitness value. A lower fitness value indicates that the balancing parameter more effectively extracts pure respiratory and cardiac signal components.

With the optimal balancing parameter obtained, the final SVMD is executed, yielding a set of intrinsic mode functions (IMFs). To accurately identify respiratory and cardiac components from these IMFs, a modal selection method is employed. This method utilizes frequency priors and MSC, operating under the assumption of time-domain stationarity for vital signs.

The modal selection procedure is as follows.

Based on physiological prior knowledge, the typical frequency of human respiratory signals ranges from 0.1 to 0.5 Hz, whereas that of cardiac signals spans 0.8 to 2 Hz.[20] The FFT is applied to the K modal components to obtain their frequency spectra. Spectral peak detection is then conducted to categorize those components with dominant frequencies within the corresponding physiological bands as candidate modes.

During continuous monitoring, the selection robustness is enhanced through the following procedure: In the initial estimation, the first candidate mode identified as the respiratory signal

is selected. For the cardiac component, a candidate mode whose dominant frequency is not a harmonic multiple of the respiratory frequency is chosen as the reference. In subsequent estimations, MSC is calculated between each candidate mode $u_k(t)$ and the reference mode $s(t)$. MSC measures the spectral similarity between two signals in the frequency domain. Its calculation formula is

$$C_{u_k,\,s}(f) = \frac{|P_{u_k,\,s}(f)|^2}{P_{u_k,\,u_k}(f)\cdot P_{s,\,s}(f)} \in [0,1], \tag{21}$$

where $P_{u_k,\,s}(f)$ is the cross-power spectral density between the two modes, $P_{u_k,\,u_k}(f)$ is the PSD of the current candidate mode $u_k(t)$, and $P_{s,\,s}(f)$ is the PSD of the reference mode $s(t)$.

The optimal candidate mode is selected by comparing the MSC values of all the candidates. If the MSC of the optimal candidate exceeds a preset coherence threshold, it replaces the current reference mode; otherwise, the original reference is retained. Should no update occur over consecutive iterations, the coherence threshold is adaptively reduced to enhance the algorithm's robustness in noisy environments. Finally, on the basis of the fundamental frequency of the selected respiratory mode, potential respiratory harmonic interference in the cardiac signal is eliminated, enabling the accurate calculation of both heart rate (*HR*) and respiratory rate (*RR*).

During continuous monitoring, a dynamic parameter update strategy balances computational efficiency with adaptability. The strategy follows a two-stage decision process: First, it determines if the newly acquired data volume is sufficient for the next estimation cycle, if so, the process continues; otherwise, it terminates. Subsequently, if the fitness value derived from the new data using the current optimal parameter remains within a preset threshold of the historical optimum, these parameters are reused directly. Otherwise, the adaptive optimization process is re-invoked to update the optimal balancing parameter. This approach ensures robust performance in time-varying interference environments while maintaining high computational efficiency.

3. Validation and Analysis

3.1 Algorithm validation

The feasibility of the proposed CSA-SVMD algorithm was validated using a practical radar system. The hardware platform employed the company's proprietary BMR2 vital sign monitoring board, which integrates TI's IWR1443 millimeter-wave radar chip and a high-performance processor. To comprehensively evaluate the performance of the proposed CSA-SVMD algorithm under multi-source dynamic interference, we recruited the ten healthy adult subjects shown in Table 1. The experiment was conducted in an environment with substantial ferrous reflectors. Each subject was tested at distances of 0.5, 0.8, and 1 m in front of the radar. During data acquisition, subjects were mostly in a normal resting state but occasionally performed slight body movements to simulate realistic interference scenarios. The radar system operated simultaneously with a three-lead multi-parameter monitor attached to the chest for reference vital sign acquisition, ensuring accurate time synchronization. As depicted in Fig. 3,

Table 1
Information of subjects.

Subject	Gender	Age	Height (cm)	Weight (kg)
1	Female	25	170	48
2	Female	24	166	55
3	Female	27	168	60
4	Female	27	156	53
5	Female	22	167	50
6	Male	36	175	76
7	Male	26	177	68
8	Male	29	178	71
9	Male	25	185	80
10	Male	24	176	75

Fig. 3. (Color online) Practical verification of CSA-SVMD algorithm.

the radar transmitted the FMCW signal towards a seated adult female subject who exhibited a slight periodic forward-backward upper-body movement. The signal impinged on the target, and the reflected echo was processed through mixing, filtering, and analog-to-digital conversion (ADC) to obtain the digital IF signal. The specific radar parameter settings are provided in Table 2.

The digital IF signal was processed by range-dimension FFT, phase arctangent demodulation, phase unwrapping, phase differencing, and Kalman filtering to obtain a phase sequence signal containing cardiac and respiratory information. The amplitude–frequency plot of this signal is shown in Fig. 4, where f_r and $2f_r$ and $3f_r$ are the respiratory fundamental frequency and its harmonics, respectively, and f_h is the cardiac fundamental frequency.

The parameters were configured as follows: population size = 5, maximum number of iterations = 15, and balancing parameter search range = [2000, 10000]. The CSA-SVMD algorithm converged to an optimal α of 7450. Figure 5 illustrates the result of a single decomposition. Using frequency priors and MSC, the respiratory mode u_1 and cardiac mode u_3 were selected, as shown in Fig. 6. This process results in the precise estimation of vital signs.

Table 2
Radar parameters.

Parameter name	Parameter value
Start frequency (GHz)	77
Bandwidth (GHz)	4
Frequency slope (MHz/μs)	70
Sample rate (ksps)	4000
ADC samples	200
Frame periodicity (ms)	50
Transmit antenna	1
Receive antenna	4

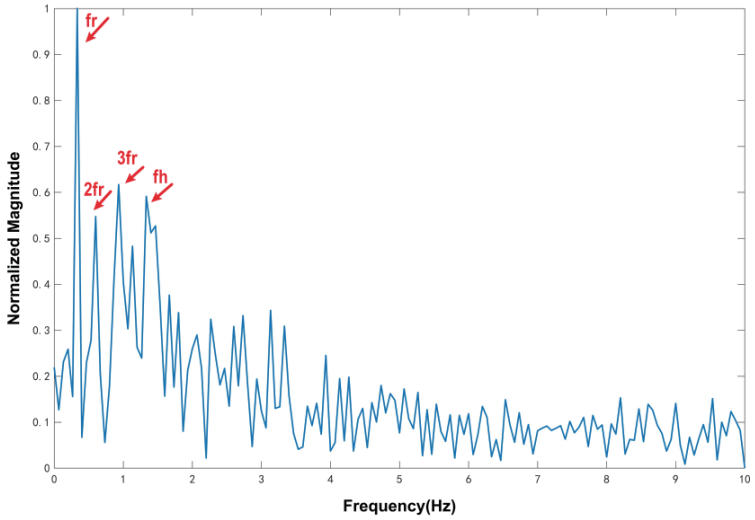

Fig. 4. (Color online) Amplitude–frequency diagram of the phase sequence signal.

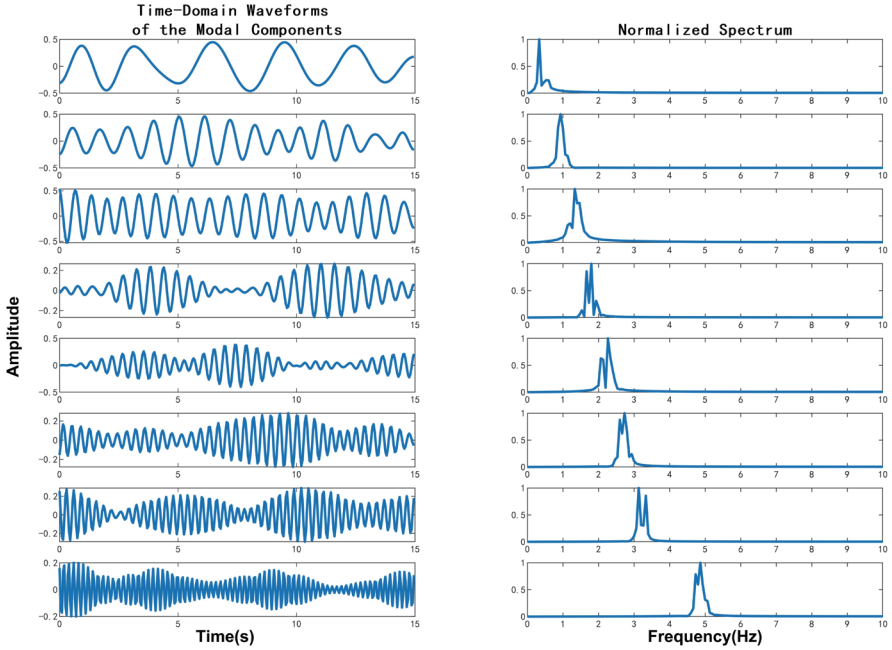

Fig. 5. (Color online) Decomposition result of CSA-SVMD.

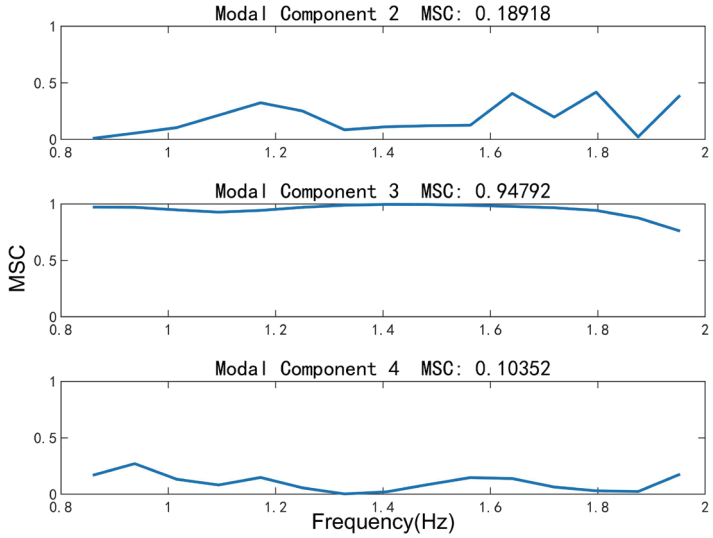

Fig. 6. (Color online) MSC comparison.

3.2 Results analysis

One minute of raw data were collected from subject 1 and processed using the following four methods: infinite impulse response (IIR) filtering, VMD (with the number of modes $K = 8$ and the penalty factor $\alpha_{vmd} = 7000$), SVMD (with the balancing parameter $\alpha_{svmd} = 7000$), and the proposed CSA-SVMD. A comparison of *HR* and *RR* estimation results is presented in Figs. 7 and 8, where the dark blue solid line denotes the reference measurements from a multi-parameter monitor, and the other colored lines represent the values estimated using the different algorithms.

The processing results were quantitatively compared using the root mean square error (*RMSE*), with the mathematical expression given in Eq. (22). Here, p_n and $\hat{p}_n$ are the nth reference and estimated values, respectively, and N is the number of samples.

$$RMSE = \sqrt{\frac{1}{N}\sum_{n=1}^{N}(p_n - \hat{p}_n)^2} \tag{22}$$

The quantitative results derived from five minutes of continuous data collection per subject at each measurement distance are summarized in Tables 3–5. As shown, across all distances, the CSA-SVMD algorithm achieves a lower *RMSE* than all other algorithms under multi-source dynamic interference. However, the estimation accuracy of all algorithms, including CSA-SVMD, decreases as the measurement distance increases, owing to the decreased signal strength and increased susceptibility to interference. Compared with the fixed-parameter reference algorithms, CSA-SVMD maintains a more stable performance degradation trend, demonstrating its stronger robustness and adaptive capability in dynamic interference scenarios.

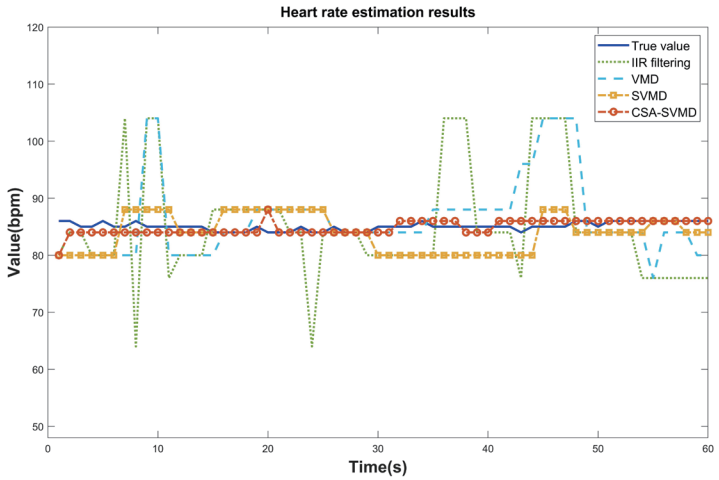

Fig. 7. (Color online) Comparison of *HR* estimation results.

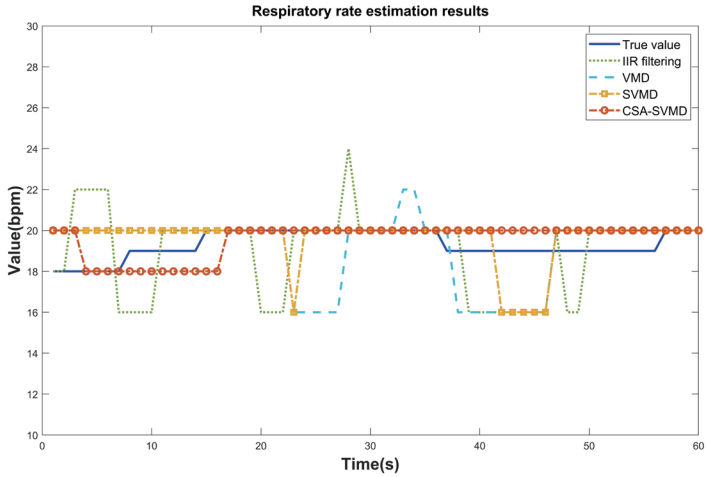

Fig. 8. (Color online) Comparison of *RR* estimation results.

Table 3
RMSE comparison of vital sign estimation at 0.5 m distance.

	IIR filtering		VMD		SVMD		CSA-SVMD	
Subject	*RR*	*HR*	*RR*	*HR*	*RR*	*HR*	*RR*	*HR*
1	2.48	12.28	2.11	8.25	1.68	6.78	1.25	2.34
2	4.13	11.24	2.26	8.45	2.14	7.64	1.64	2.83
3	2.87	12.34	2.65	7.68	2.51	7.42	1.47	2.14
4	4.80	12.35	3.42	8.54	2.81	6.05	2.01	2.55
5	3.75	13.31	2.79	7.88	1.78	7.74	1.65	2.29
6	3.32	11.13	2.21	8.75	2.05	6.48	1.33	1.54
7	4.52	14.13	2.47	7.36	2.08	7.16	1.57	2.82
8	4.91	11.41	4.25	9.04	3.14	7.79	2.12	3.06
9	3.64	11.10	3.51	7.24	2.21	6.12	1.08	1.28
10	4.22	13.75	2.80	7.86	1.95	5.14	1.92	1.34

Table 4
RMSE comparison of vital sign estimation at 0.8 m distance.

	IIR filtering		VMD		SVMD		CSA-SVMD	
Subject	*RR*	*HR*	*RR*	*HR*	*RR*	*HR*	*RR*	*HR*
1	3.93	13.65	2.25	8.68	1.95	8.09	1.84	3.59
2	4.89	13.39	2.71	10.57	2.23	9.17	1.78	3.35
3	5.95	13.24	3.82	9.14	2.76	7.48	2.32	2.78
4	4.64	14.07	4.49	9.07	3.14	6.09	2.45	3.14
5	4.15	13.59	3.67	8.92	3.05	8.83	1.85	3.85
6	5.24	14.87	2.92	10.24	2.66	8.24	1.47	2.07
7	5.98	14.45	3.47	7.98	2.45	7.41	2.34	4.12
8	5.47	12.56	4.79	10.12	3.07	8.04	3.03	3.58
9	4.09	11.94	3.14	8.06	2.41	7.86	1.97	3.25
10	4.37	13.77	2.98	8.67	2.33	6.95	2.16	1.87

Table 5
RMSE comparison of vital sign estimation at 1.0 m distance.

	IIR filtering		VMD		SVMD		CSA-SVMD	
Subject	*RR*	*HR*	*RR*	*HR*	*RR*	*HR*	*RR*	*HR*
1	4.78	14.70	3.65	10.65	3.78	8.87	2.20	4.52
2	5.02	15.39	4.39	12.47	3.86	10.49	2.15	5.26
3	5.87	14.35	4.79	10.85	4.23	8.25	2.38	3.24
4	5.36	15.28	4.61	11.92	4.15	9.29	2.68	4.76
5	6.17	16.26	4.51	12.03	3.82	9.28	2.60	5.14
6	5.36	15.33	4.88	12.87	3.21	10.25	3.04	5.95
7	5.79	15.47	3.92	13.15	3.09	10.17	2.65	5.60
8	5.63	15.04	4.90	11.78	3.67	8.58	3.66	4.13
9	5.48	14.59	4.71	12.06	3.34	8.45	2.16	4.97
10	5.15	14.74	4.43	13.22	3.51	8.64	2.81	5.72

4. Conclusions

To address the challenges of low accuracy and robustness in millimeter-wave radar vital sign sensing data estimation under multi-source dynamic interference scenarios, we propose the CSA-SVMD algorithm in this paper. The core of our approach involves constructing a fitness function derived from the time-frequency features of vital signs and leveraging the CSA to adaptively optimize the balancing parameters of SVMD. Precise estimation is ultimately achieved by incorporating frequency priors and magnitude-squared coherence. Extensive experiments were conducted using the BMR2 vital sign monitoring board with ten healthy subjects of varying physiques, tested at distances of 0.5, 0.8, and 1.0 m. The results demonstrate that CSA-SVMD significantly outperforms IIR filtering, VMD, and conventional SVMD. Specifically, at 0.5 m, the *RMSE* between reference values and CSA-SVMD estimates falls predominantly within 2 beat per minute (bpm) for RR and 3 bpm for HR across all subjects. Although *RMSE* increases with measurement distance, with the average HR error rising from approximately 3 bpm at 0.5 m to about 5 bpm at 1.0 m across subjects, CSA-SVMD maintains the lowest error and the most gradual performance degradation compared with other algorithms.

The experimental results show the superior accuracy of CSA-SVMD, which achieved significantly lower estimation errors across all subjects and distances. While all methods showed an increased error as the measurement range extended, CSA-SVMD maintained the most stable and gradual performance degradation, confirming its reliable adaptability in multi-source dynamic interference scenarios. Furthermore, it performed consistently across subjects of different genders and body types, underscoring its strong generalizability. The incorporation of a dynamic parameter update strategy ensures the algorithm's adaptability and reliability during continuous monitoring in time-varying real-world scenarios, thereby providing a robust technical solution for the long-term health monitoring of special populations, such as burn patients and the elderly with limited mobility. The proposed method holds strong potential for future expansion into multi-target monitoring and clinical validation. Furthermore, its core framework (adaptive parameter optimization via meta-heuristic algorithms) could be extended to enhance accuracy at longer distances, for instance, by exploring the fusion of CSA with other optimizers in a hybrid framework or by incorporating spatial filtering algorithms to improve signal-to-noise ratio in challenging propagation conditions.

Acknowledgments

This work was supported by the 2025 Tianjin Municipality Key R&D Program–R&D Special Project for the Science and Technology Service Industry (25YFKFYS00430).

References

1 K. Gupta, M. B. Srinivas, J. Soumya, O. J. Pandey, and L. R. Cenkeramaddi: IEEE Sens. J. **22** (2022) 22179. https://doi.org/10.1109/JSEN.2022.3210256
2 S. Y. Li, G. Y. Liu, P. X. Hu, P. S. Li, D. Y. Xu, and Z. Wang: IEEE Access **13** (2025) 163907. https://doi.org/10.1109/ACCESS.2025.3609787
3 Y. Jing, Y. L. Yan, Z. Li, F. G. Qi, T. Lei, J. Q. Wang, and G. H. Lu: Sensors **25** (2025) 5232. https://doi.org/10.3390/s25175232
4 Y. C. Xie and B. Guo: Sensors **25** (2025) 5620. https://doi.org/10.3390/s25185620
5 K. K. Vincent, L. Wang, and W. Y. Liu: IEEE Trans. Consum. Electron. **70** (2023) 2970. https://doi.org/10.1109/TCE.2023.3321683
6 T. K. V. Dai, Y. Yu, P. Theilmann, A. E. Fathy, and O. Kilic: IEEE J. Electromagn. RF Microwaves Med. Biol. **6** (2022) 429. https://doi.org/10.1109/JERM.2022.3140900
7 N. E. Huang, Z. Shen, S. R. Long, M. C. Wu, H. H. Shih, Q. Zheng, N. C. Yen, C. C. Tung, and H. H. Liu: Proc. R. Soc. London, Ser. A. **454** (1998) 903. https://doi.org/10.1098/rspa.1998.0193
8 K. Dragomiretskiy and D. Zosso: IEEE Trans. Signal Process. **62** (2013) 531. https://doi.org/10.1109/TSP.2013.2288675
9 M. M. Arslan, S. U. Rahman, A. A. Shah, N. Zhao, Z. Y. Zhang, and T. Cui: IEEE Sens. J. **25** (2025) 20374. https://doi.org/10.1109/JSEN.2025.3558625
10 M. Li, Y. Luo, and X. Z. Ke: J. Comput. Appl. **44** (2024) 1978. https://doi.org/10.11772/j.issn.1001-9081.2023060737
11 M. Y. Zuo: Proc. 2025 4th Int. Symp. Computer Applications and Information Technology (ISCAIT, 2025) 2013. https://doi.org/10.1109/ISCAIT64916.2025.11010615
12 D. H. Li, Y. K. Huang, H. Q. Li, J. R. Cheng, W. W. Zhu, and H. M. Feng: IEEE Sens. J. **25** (2025) 13937. https://doi.org/10.1109/JSEN.2025.3542776
13 M. Nazari and S. M. Sakhaei: Signal Process. **174** (2020) 107610. https://doi.org/10.1016/j.sigpro.2020.107610
14 M. S. Braik: Expert Syst. Appl. **174** (2021) 114685. https://doi.org/10.1016/j.eswa.2021.114685
15 G. Paterniani, D. Sgreccia, A. Davoli, G. Guerzoni, P. D. Viesti, and A. C. Valenti: Proc. IEEE **111** (2023) 277. https://doi.org/10.1109/JPROC.2023.3244362

16 P. Duhamel and M. Vetterli: Signal Process. **19** (1990) 259. https://doi.org/10.1016/0165-1684(90)90158-U
17 L. H. Qiao, Z. H. Wang, B. Xiao, Y. C. Shu, X. Luan, and Y. H. Shi: IEEE Trans. Instrum. Meas. **72** (2023) 1. https://doi.org/10.1109/TIM.2023.3274171
18 S. Malekpour, J. A. Gubner, and W. A. Sethares: J. Franklin Inst. **355** (2018) 2932. https://doi.org/10.1016/j.jfranklin.2018.01.014
19 R. N. Youngworth, B. B. Gallagher, and B. L. Stamper: Proc. Optical Manufacturing and Testing VI (SPIE, 2005) 58690U. https://doi.org/10.1117/12.618478
20 B. R. Upadhyay, A. B. Baral, and M. Torlak: IEEE Access **10** (2022) 106017. https://doi.org/10.1109/ACCESS.2022.3211527